The Effect of Confinement on the Structure–Conductivity Relationship in PEO/LiTFSI Electrolytes in 3D Microporous Scaffolds

Shreyas Pathreeker[1], Hyeongjun Koh[1], Weiwei Kong[1], Richard Robinson[2], Gillian Weissman[2], Eric A. Stach[1], Eric Detsi[1], Prof. Russell J. Composto*, [1, 3]

[1]Department of Materials Science and Engineering, School of Engineering and Applied Science, University of Pennsylvania, Philadelphia, PA, 19104, United States

[2]Xerion Advanced Battery Corporation, Kettering, OH, United States

[3]Department of Chemical and Biomolecular Engineering, School of Engineering and Applied Science, University of Pennsylvania, Philadelphia, PA, 19104, United States

*Corresponding author: composto@seas.upenn.edu

Abstract

Because 3D batteries comprise solid polymer electrolytes (SPE) confined to high surface area porous scaffolds, the interplay between polymer confinement and interfacial interactions on total ionic conductivity must be understood. This paper investigates contributions to the structure-conductivity relationship in poly(ethylene oxide) (PEO)–lithium bis(trifluorosulfonylimide) (LiTFSI) complexes confined to microporous nickel scaffolds. For bulk and confined conditions, PEO crystallinity decreases as the salt concentration (Li^+:EO (r) = 0.0.125, 0.0167, 0.025, 0.05) increases. For pure PEO and all r values except 0.05, PEO crystallinity under confinement is lower than in the bulk, whereas glass transition temperature remains statistically invariant. At 298 K (semicrystalline), total ionic conductivity under confinement is higher than in the bulk at $r = 0.0167$, but remains invariant at $r = 0.05$; however, at 350 K (amorphous), total ionic conductivity is higher than in the bulk for both salt concentrations. Time–of–flight secondary ion mass spectrometry indicates selective migration of ions towards the polymer–scaffold interface. In summary, for the 3D structure studied, polymer crystallinity, interfacial segregation, and tortuosity play an important role in determining total ionic conductivity and, ultimately, the emergence of 3D SPEs as energy storage materials.

Main Text

Three–dimensional solid–state batteries (3D SSBs) offer significant advantages over conventional 2D batteries, namely, high areal energy and power densities due to their increased surface area and intimate contact between cell components. 3D SSBs comprise porous 3D scaffolds that confine solid polymer electrolytes (SPEs)[17] to form dense composites with extensive scaffold–SPE interfaces. Polymer confinement is a topic of intense fundamental research because confinement can modulate the polymer glass transition temperature (T_g),[1–5] segmental relaxation rate,[6–8] chain conformation,[9, 10] polymer crystallinity (X_c),[11–13], viscosity,[14] and thermal stability.[15, 16] Total ionic conductivity (σ) of SPEs, an important electrochemical property, also depends upon polymer structure, thereby making 3D confined SPEs of interest both fundamentally and for energy storage applications.

Poly(ethylene oxide) (PEO)–based SPEs are popular due to the high dielectric constant (ε) of PEO[18] and its ease of processability. Yet, practically–useful σ values on the order of 10^{-3} S/cm[19, 20] become achievable only at $T > T_m$ (polymer melting point) and/or at high salt concentrations, often at the cost of the SPE modulus. Confining PEO SPEs within robust porous media is a practical engineering strategy to balance the trade–off between mechanical properties and σ. In this study, the σ of PEO SPEs is directly impacted by 5 key contributors: 1.) T_g, 2.) X_c, 3.) ion transport pathways (pore tortuosity, τ_P), 4.) free charge carrier concentration (n_{free}), and 5.) lamellar tortuosity (τ_L).[21] Pore tortuosity is generated by the pore network, whereas lamellar tortuosity is generated by the PEO lamellae. These contributors often affect σ orthogonally to one another: increasing salt concentration leads to a higher n_{free} but also a higher T_g, which suppresses polymer (and thus ion) mobility. Analogously, addition of filler suppresses X_c and increases the volume fraction of amorphous polymer, but may increase T_g and reduce n_{free} thereby suppressing σ. Thus far, the majority of studies on 3D confined SPEs has focused on optimizing SPE electrochemical performance by tuning scaffold properties: surface chemistry, pore connectivity, and porosity, but typically at a fixed salt concentration.[22] As such, a systematic fundamental investigation of structure–property relationships in 3D confined SPEs is lacking. Further, experimentally–observed improvements in σ are often simply attributed to changes in X_c, and the influence of the remaining contributors on σ remains unclear. In this fundamental study, we systematically probe how polymer thermal properties, namely T_g and T_m, structure (X_c), and pore tortuosity τ_P affect σ in confined PEO–lithium bis(fluorosulfonylimide) (LiTFSI) electrolytes. We propose that ion–scaffold interactions can also play a role in determining n_{free}. Given the large surface area of the porous 3D scaffolds, even weak interactions can reduce σ.

Porous nickel (Ni) scaffolds (thickness ~80 μm thick, pore diameter ~2 μm–10 μm, pore volume ~75%, i.e., $\Phi = 0.75$) were used as confining matrices. The microporous Ni scaffold used in this work is a novel, highly–tunable battery electrode architecture currently used for silicon anode applications in lithium–ion batteries. Confined SPEs were prepared using capillary–rise–infiltration (CaRI) of polymer electrolyte melts into porous scaffolds as depicted in **Figure 1**, which shows a fracture surface of pristine porous scaffold in cross–section. CaRI is based on capillary action wherein favorable wetting of the porous scaffold surface by a wetting fluid (in this case the melt) results in drawing of the melt into the scaffold.[5, 6, 15, 23, 24] The exact preparation procedure can be found in **Section S1**. The maximum time required for complete infiltration at T = 120°C was estimated from the classical Lucas–Washburn equation[5, 25, 26] as 38 minutes for pure PEO melt (**Section S1**). Since the actual exposure time was 3 hours, we expect good filling of the pores with SPE. The final composites comprise both the confined SPE and the porous scaffold together, which we hereafter refer to as polymer electrolyte composites (PECs).

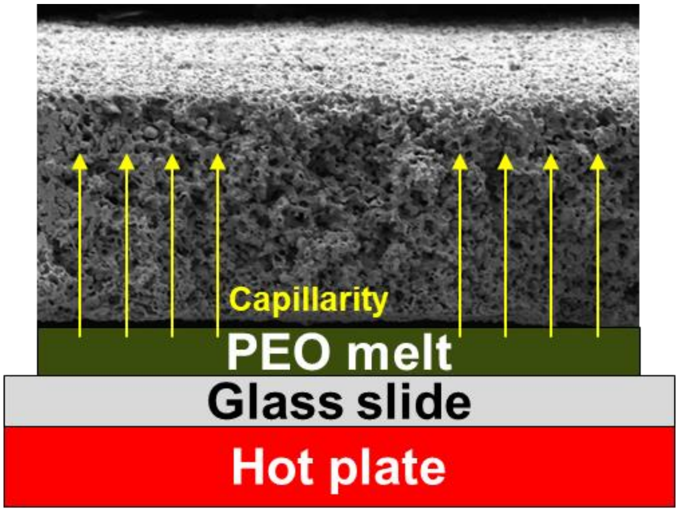

Figure 1. The CaRI fabrication process used for preparing PEO–infiltrated scaffolds (i.e., polymer electrolyte composites, PECs). The thickness of the PEC is ca. 80 μm. The SEM image shows the cross–section of an as–received porous scaffold prior to polymer infiltration. Not to scale.

We used scanning electron microscopy (SEM) and energy–dispersive x–ray spectroscopy (EDS) to characterize the PECs after cooling and crystallization as shown representatively in **Figure 2**. Figure 2a) and Figure 2c) show SEM images of a representative PEC at high and low magnifications, respectively. Corresponding EDS maps are shown in Figure 2b) and Figure 2d).

Collectively, this data reveals a dense composite comprising polymer (green) and scaffold (gray). Dark spots do not necessarily represent voids, but rather originate from regions with low counts due to the depth–limitation of EDS. Of note is the polymer signal observed at the unexposed (top) surface shown in Figure 2c) and Figure 2d), which highlights the efficacy of CaRI in the development of high–loading, thick polymer composites. Additional SEM images can be found in **Figure S1**. Importantly, we observe uniform pore filling in all samples which confirms the physical confinement of the SPEs within the pores of the scaffold.

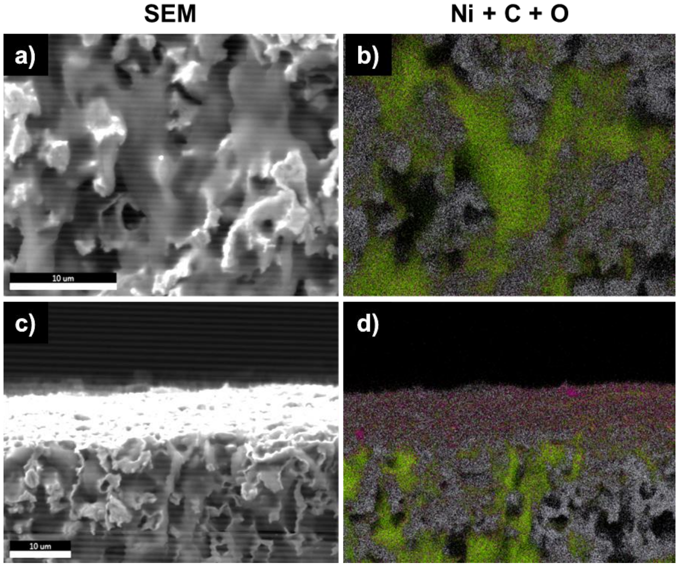

Figure 2. Representative SEM images and corresponding EDS maps of a PEC. Gray represents Ni (scaffold), green represents carbon (polymer), and pink represents oxygen. Both scale bars shown are 10 μm and also apply to their corresponding EDS maps.

Next, T_g, T_m, and X_c in the bulk and under confinement were investigated using differential scanning calorimetry (DSC). These values were extracted from raw DSC heating curves (**Figure S2** and **Figure S3**), and are summarized in **Figure 3**. In the bulk, T_g for pure PEO is ca. –55°C and increases with increasing salt concentration. At the highest salt concentration of $r = 0.05$, bulk T_g reaches ca. –45°C. PECs ((hatched gold bars, Figure 3a)) also show this trend but the changes from one salt concentration to the next are smaller in magnitude. Further, the largest difference in T_g is seen going from pure PEO to $r = 0.05$ as is also the case with the bulk SPEs. At any r value, the effect of confinement on polymer T_g is statistically insignificant relative to the bulk, suggesting that confinement of SPE to the porous scaffold does not significantly affect polymer T_g. Noticeable changes in T_g are typically observed when the length scale of confinement approaches the polymer radius of gyration (R_g). The characteristic length scale of confinement in the present study is defined by the pore size (few μms), which is >> polymer R_g (~tens of nms). This is likely why no significant effect on T_g is seen at this confinement length scale. A comparison of the trends in these two systems, i.e., bulk vs. confined, reveals that the effect of salt addition on T_g is more pronounced in the bulk than in the PECs. A plausible explanation for this difference is ion–scaffold interactions in the PECs which will be discussed in the context of σ.

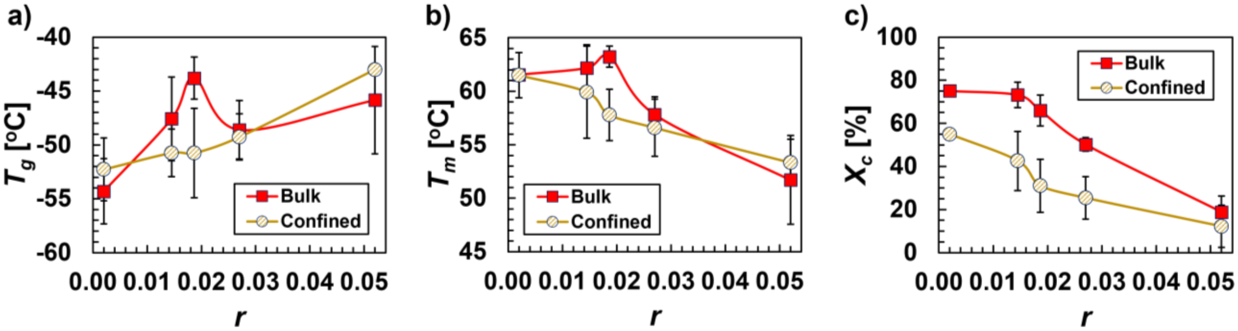

Figure 3. Summarized values of a) T_g, b) T_m, and c) X_c. All error bars represent one standard deviation from the mean of 3 separate trials except for the PEO control.

The effect of confinement and salt concentration on T_m is summarized in Figure 3b). In the bulk, increasing salt concentration leads to a decrease in T_m from ca. 62°C to ca. 52°C, and is attributed to more polymer–salt interactions and consequent disruption of X_c. The PECs also show a similar trend, and at all salt concentrations except $r = 0.05$ show a decrease in T_m relative to their bulk counterparts. Statistically, however, these changes are insignificant. The heating curves shown in **Figure S2**) indicate that the melt transition peak for every PEC becomes broader relative to that in the bulk, suggesting that the distribution of PEO lamellae sizes becomes broader under confinement, which may be attributed to the range of pore sizes in the scaffold. Thus, the melt transition in the PECs occurs over a broad temperature range with smaller crystallites melting first and larger ones melting later, reflected as broad peaks in the DSC traces.

Last, we investigate the effect of confinement and salt concentration on X_c (Figure 3c)). X_c for bulk PEO is around 78%, and decreases gradually as salt concentration increases. At the highest salt concentration of $r = 0.05$, X_c reduces to ca. 20% in the bulk. The PECs exhibit a similar trend. This reduction in X_c with increase in salt concentration is attributed to coordination of the PEO chains with Li^+ cations from dissociated salt.[s] An increase in salt concentration and reduction in X_c in the bulk SPEs were also confirmed using vibrational spectroscopy and optical microscopy, respectively (**Figure S4** and **Figure S5**). The PECs exhibit a lower X_c relative to their bulk counterparts except for the $r = 0.05$ case where X_c remains statistically invariant. The largest changes are observed for the dilute systems, suggesting that the effect of physical confinement on the SPEs is salt–concentration–dependent. Dilute systems likely experience a stronger effect from confinement (30% to 40% reduction in X_c) whereas more concentrated ones do not (<20% reduction in X_c). It stands to reason that polymer–ion interactions may dominate at higher salt concentrations, thereby explaining this trend. These trends also agree well with the corresponding T_m trends. Further, the volume fraction of polymer in the PECs is ca. 75%. If there were no effect on confinement on X_c, then $X_{c\text{–}confined}$ should be reduced by 25% relative to $X_{c\text{–}bulk}$. However, we find that the ratio $X_{c\text{–}confined}/X_{c\text{–}bulk}$ is < 0.75, suggesting that the lower X_c in the PECs is not simply a function of the pore volume but rather a consequence of physical confinement of the PEO spherulites. We posit that the PEO crystallization is frustrated under confinement due to restricted spherulite growth. Melt–crystallized PEO spherulites are typically on the order of hundreds of μm in the bulk (**Figure S4**). When the polymer melt crystallizes within pores of size ca. 5 μm, growth of its spherulitic domains is constrained by the pores, thereby lowering X_c in the PECs. Transmission WAXS results on selected bulk SPEs and PECs also corroborate these findings from DSC analysis (**Figure S6**).

Classical free–volume theory has established that ion transport occurs primarily in the amorphous phase of an ionically conducting polymer.[27] To understand the correlation between X_c and total ionic conductivity, electrochemical impedance spectroscopy (EIS) was carried out to determine the σ of the bulk SPEs and PECs at 298 K and 350 K, corresponding to semicrystalline and amorphous morphologies, respectively. Since moisture directly affects ionic conductivity,[28] care was taken to carry out all measurements under vacuum. σ_{bulk} as a function of salt concentration is shown in **Figure S7**. At 298 K, σ_{bulk} for $r = 0.05$ is 2.3 x 10^{-6} S/cm, similar to that reported by Devaux et al. (MW$_{\text{PEO}}$ = 35 k*Da*, $r = 0.04$)[29] and slightly lower than that reported by Zhang et al. (MW$_{\text{PEO}}$ = 500 k*Da*, $r = 0.05$).[30] σ_{bulk} values for $r = 0.0125, 0.0167$, and 0.025 are ca. 5.0 x 10^{-7} S/cm, i.e., an order of magnitude lower than the (20:1) case. This reduction is expected due to decrease in the number of free charge carriers and increase in X_c with decreasing salt concentration. Because all SPEs are amorphous at 350 K (see phase diagram in **Figure S8**), σ is decoupled from the effects of polymer crystallinity. At 350 K, σ_{bulk} lies between 1.5 x 10^{-4} S/cm and 7.4 x 10^{-4} S/cm, in good agreement with values reported by Lascaud et al. (MW$_{\text{PEO}}$ > 3.9 k*Da*),[18] Mongcopa et al. (90°C, MW$_{\text{PEO}}$ = 35 k*Da*),[31] and Pesko et al. (90°C, MW$_{\text{PEO}}$ = 5 k*Da* and MW$_{\text{PEO}}$ = 275 k*Da*).[32] Our ionic conductivity value for $r = 0.05$ at 350 K (7.4 x 10^{-4} S/cm) is in the vicinity of that reported by Zhao et al.[33] (~8 x 10^{-4} S/cm, MW$_{\text{PEO}}$ 5000 k*Da*), Xiong et al.[34] (7.5 x 10^{-4} S/cm,

MW_{PEO} = 1000 k*Da*), and within the expected value based on results from Hoffman et al.[35] However, although σ increases as salt concentration increases, this increase is quite small at dilute salt concentrations, as also reported by Pesko et al.[32] Therefore, we chose to compare σ at two salt concentrations – $r = 0.0167$ representing a dilute SPE and $r = 0.05$ representing a concentrated SPE. Note that insulating polymer layers of poly(vinylidene fluoride)–co–hexafluoropropylene (PVDF–co–HFP) were applied to the top and bottom of the PECs to prevent short circuit. The corresponding EIS setup can be found in **Figure S9**, along with a description of possible charge flow through the trilayer system in **Figure S10**. The geometry and stability of the insulating layers were verified using SEM after EIS measurements at 350 K and cooling to the ambient, shown representatively in **Figure S11**. Raw Bode plots from EIS can be found in **Figure S12**, wherein the inert nature of PVDF–co–HFP leads to only a single relaxation process from the PECs. We also carried out EIS on a bulk SPE ($r = 0.05$, 298 K) sandwiched between the PVDF–HFP overlayers, and found the ionic conductivity to be similar to that measured without the overlayers (see **Figure S13**).

We next compare the bulk and confined total ionic conductivity at dilute ($r = 0.0167$) and more concentrated ($r = 0.05$) salt concentrations as summarized in **Figure 4**. At 298 K (Figure 4a), the total ionic conductivity of the confined SPE is greater than the bulk value by 2.4x for $r = 0.0167$, whereas for $r = 0.05$, the total ionic conductivities of the bulk and confined SPEs are similar. To explain these results, we turn to polymer crystallinity analysis. X_c is ca. 66% for the bulk $r = 0.0167$ SPE, and decreases to ca. 31% under confinement. This reduction in X_c leads to a higher content of amorphous polymer, which explains the higher σ under confinement. For $r = 0.05$ SPE, X_c does not change under confinement relative to the bulk, and σ remains unchanged. The finding that a 35% reduction in X_c for the dilute salt concentration results in only a small change in $\sigma_{confined}$ vs. σ_{bulk} suggests that X_c is not the sole contributor responsible for ion transport in such composite SPEs.

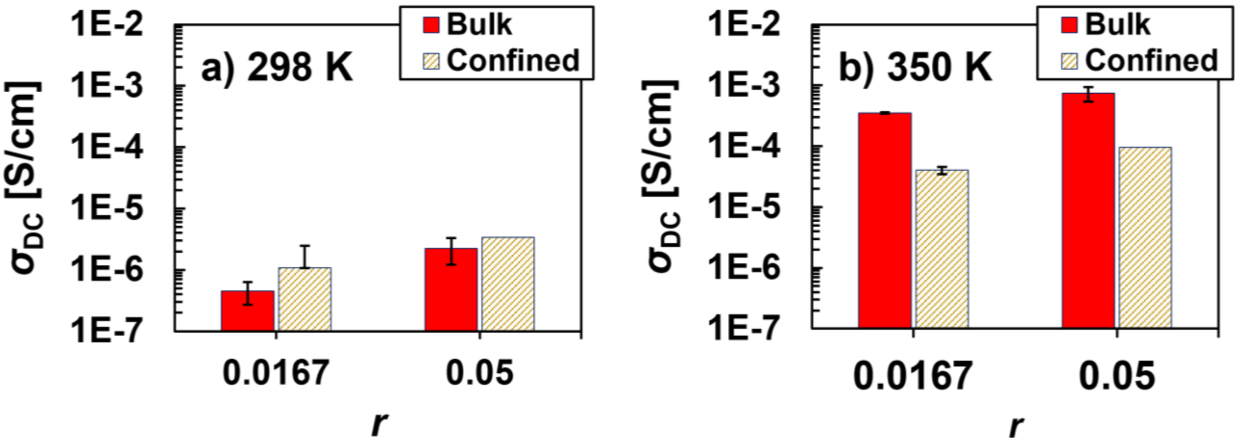

Figure 4. Bar plots showing the total ionic conductivity σ as a function of (EO:Li$^+$) ratio at a) 298 K and b) 350 K. Values are averages of at least two separate trials except for the (20:1) PEC, and error bars shown represent one standard deviation of the mean.

At 350 K (amorphous) for both PECs, Figure 4b) shows that σ of the confined SPEs is less than that of the bulk SPE by a factor of 7x to 8x. Further, for the bulk SPEs, the ratio $\sigma_{350K}/\sigma_{298K}$ is ca. 550 whereas it is only ca. 32 under confinement (PECs). To account for ionically inaccessible metal scaffold, $\sigma_{confined}$ of an electrolyte confined to a scaffold with pore volume fraction (Φ) follows $\sigma_{confined} = \Phi \times \sigma_{bulk}$, assuming an amorphous polymer matrix. To account for the non–linear pathways in the scaffold, an empirical correction factor can be incorporated, namely the pore tortuosity τ_P. The bulk and confined samples are expected to have similar free volume due to the invariance in T_g under confinement, which allows for estimation of τ_P using σ_{bulk} and $\sigma_{confined}$. All $\sigma_{confined}$ values were obtained after correcting for volume fraction of ion–conducting phase in the PECs. The typical value for τ_P in porous media lies between 1.5 and 3.0,[36, 37] whereas the value we calculated is on average 6.2 for both PECs. As such, tortuosity alone is unable to account for the lower total ionic conductivity in the PECs. Calculating tortuosity requires that there are no changes to the electrolyte (X_c, T_g) under confinement. The confined polymer electrolytes satisfy this condition at 350 K because DSC–derived T_g values under confinement are invariant relative to the bulk, and because all samples are amorphous at this temperature thereby allowing estimation of tortuosity. On the other hand, the confined polymer electrolytes are semicrystalline at room temperature adding additional tortuosity, preventing reliable estimation of tortuosity values. This deviation motivated us to consider scaffold–ion interactions, which can directly impact the number of free charge carriers n_{free} and consequently σ.

To this end, we carried out *ex–situ* ToF–SIMS on a representative PEC ($r = 0.0167$). **Figure 5a)** shows the secondary electron image of the PEC cross–section obtained after ion beam–milling and polishing. The milling was necessary to obtain a flat surface suitable for ToF–SIMS data collection. Further, polishing the milled surface using the ion beam helps removes residue and clean the surface.

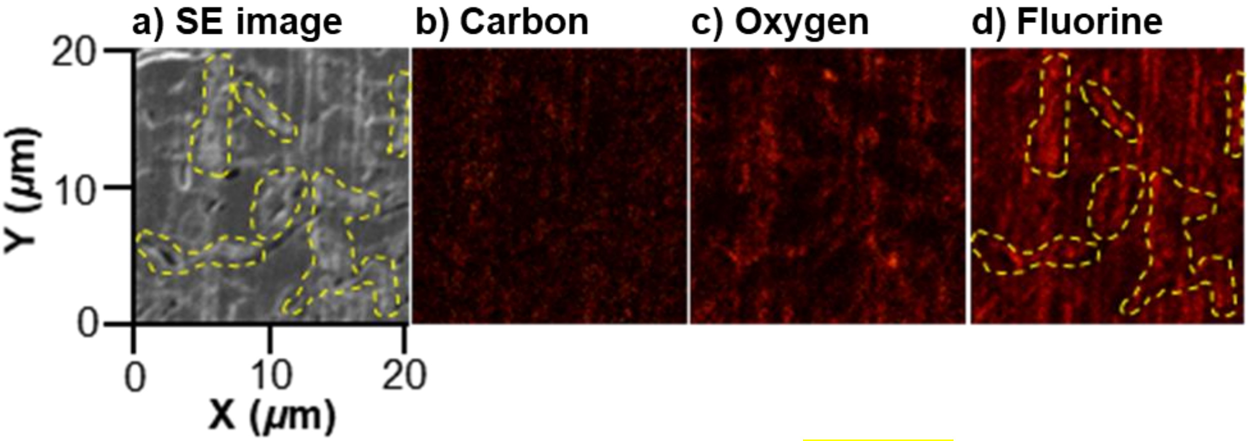

Figure 5. a) Secondary electron micrograph of the PEC (*r* = 0.0167) cross–section; b)–d) corresponding elemental maps in the X–Y plane. The milling depth corresponds to 50 frames in the thickness direction, i.e., ca. 10 μm deep. Data was collected at room temperature.

Light gray (i.e., bright) regions represent the Ni scaffold whereas dark gray (i.e., dark) regions represent the polymer electrolyte, similar to the SEM images shown in **Figure 2** and **Figure S1**. We observe a dense composite featuring continuous scaffold–polymer interfaces throughout. However, curtaining stripes, which are artifacts of the milling process, appear due to the inhomogeneous composition of the materials.[38] These striped regions cause excessive signals in TOF–SIMS, which is unavoidable due to the faster milling rate in the protruding areas compared to the adjacent flat regions. This differential milling rate in the stripes leads to the generation of more secondary ions when the region of interest is milled.[39] For this reason, we delineate the regions of interest from the curtaining stripes using dashed yellow lines. Corresponding elemental maps in the X–Y plane are shown in **Figure 5b)–Figure 5d)**. The source of these elements is the polymer electrolyte, with both PEO and LiTFSI contributing to the C and O signals. The only source of F in the PEC is the TFSI$^-$ anion. The distribution of C (Figure 5b)) is more uniform relative to O and F, although there are some dark patches observed. Note that the intensities from these dark regions are non–zero, and the apparent micron–scale variations originate from the different surface roughness generated by the differential milling rates between the hard metal scaffold and soft polymer electrolyte. On the other hand, we observe in Figure 5c) and Figure 5d) that the O and F signals are more localized towards the scaffold surfaces, resulting in 'hotspots' that overlap with the underlying SE image shown in Figure 5a). The F/C and F/O ratio maps (see

Figure S14) also show hotspots of fluorine in the vicinity of the scaffold–polymer interface. Since the bright regions in panel a) represent the Ni scaffold, this observation suggests the segregation of $TFSI^-$ towards the scaffold surface leading to a large F signal despite the crystalline PEO on the scaffold possibly limiting direct scaffold–ion interactions. As such, we expect amplification of this phenomenon in the melt wherein the scaffold surface is more accessible to the ions. The individual mass spectra from representative bright and dark regions (see **Figure S15**) suggest that the fluorine intensity in the bright region is ca. 3x that in the adjacent dark region. Note that no evidence of nickel oxide was found in the ToF–SIMS mass spectra.

Experimental evidence for selective LiTFSI adsorption in anodized aluminum oxide (AAO) pores has also been presented in the literature.[40] Further, our raw mass spectra indicate a 96x higher concentration of F in the PEC relative to the empty Ni scaffold (see **Figure S16**). The signals are orders of magnitude higher than the background, eliminating the possibility of the signals being noise. Collectively, these observations point to the possibility of selective salt adsorption to the scaffold surface thereby reducing $\boldsymbol{n_{free}}$ available for ion transport, consequently lowering σ in the PECs at 350 K. Such a mechanism can also explain the weaker dependence of T_g on salt concentration observed in Figure 3. The insulating overlayers used for EIS of the PECs are not expected to contribute to salt partitioning since PVDF–co–HFP does not dissolve LiTFSI well.[41]

Based on these findings, we propose a comprehensive picture of total ionic conductivity in high–loading composite polymer electrolytes. $\sigma_{confined}$ is governed by a balance between reduction in X_c and adsorption of salt to the scaffold surface depending upon salt concentration. At a dilute salt concentration at 298 K, the expected increase in $\sigma_{confined}$ due to reduction in X_c is observed. At a moderate salt concentration at 298 K, the reduction in X_c from confinement is insufficient to improve $\sigma_{confined}$. At 350 K, salt adsorption and pore tortuosity primarily govern $\sigma_{confined}$ and the PECs are less ionically conductive than their bulk counterparts at both salt concentrations. Higher polymer mobility at the higher temperature allows more ion–scaffold interactions, which likely amplifies the effect of the interface. Recent experimental work by Tekell et al.[42], and computational work on high–loading SiO_2–PEO electrolyte melts by Martin Dalmas[43] both suggest that in the melt σ decreases in the presence of filler because the total ionic conducting phase (polymer) is replaced by non–conducting phase (filler). Our findings qualitatively agree with these reports.

In conclusion, our results highlight the impact of the confining medium on ion transport properties. Out of the 5 factors outlined initially (polymer glass transition temperature T_g, polymer crystallinity X_c, pore tortuosity τ_P, free ion concentration n_{free}, and lamellar tortuosity τ_L, we find that the glass transition temperature does not change significantly at this length scale of confinement. At room temperature, polymer crystallinity alone is insufficient to explain the changes observed in total ionic conductivity. Decoupling of polymer crystallinity from ionic conductivity above T_m suggests that pore tortuosity and ion–scaffold interactions are the more important factors. However, pore tortuosity only partially explains the reduced total ionic conductivity observed under confinement. Time–of–flight secondary–ion mass spectrometry (ToF–SIMS) suggests selective segregation of dissociated ions towards the scaffold, which we posit leads to a lower effective free charge carrier concentration. Therefore, total ionic conductivity is governed by a combination of polymer crystallinity, pore tortuosity, and ion–scaffold interactions. Our findings are especially relevant to 3D solid–state–batteries wherein polymer electrolytes are filled into porous scaffolds with large surface areas, and interfacial effects can dominate. In such dense composites, the role of the filler should be accounted for while determining overall electrochemical performance. At room temperature, PEO lamellar tortuosity inside the pore network is expected to cause conductivity anisotropy.[11, 21] Also important is the degree of connectivity of the pores in the scaffold. To this end, isothermal polymer crystallization studies in controlled porous materials are in progress and will be reported in the future.

Supporting Information

Experimental section; Calculation of polymer infiltration time; Cross–sectional scanning electron micrographs of PECs; Raw DSC curves; Differential DSC curves; Optical micrographs; FTIR spectra; Wide–angle x–ray scattering (WAXS) plots; Total ionic conductivity plot; DSC–derived phase–diagram; Schematic of PEC EIS cell configuration; Proposed schematic and description of EIS through trilayer system; Cross–sectional scanning electron micrographs of PEC trilayer composites; Representative Bode plots from EIS measurements; Comparative Bode plots between regular and trilayer configuration; ToF–SIMS ratio maps; Selected ToF–SIMS mass spectra; Raw ToF–SIMS mass spectra for empty scaffold and a PEC.

Acknowledgements

The authors gratefully acknowledge financial support from the National Science Foundation (NSF) under Future Manufacturing grant NSF–FMRG–2134715 (SP, RJC, EAS, ED), the Division of Materials Research Polymers Program under grants NSF–DMR–1905912 (RJC) and NSF–DMR–2407300 (RJC). The authors acknowledge use of the Dual Source and Environmental X–Ray Scattering facility operated by the Laboratory for Research on the Structure of Matter at the University of Pennsylvania (NSF–MRSEC–DMR–2309043). This work was carried out in part at the Singh Center for Nanotechnology at the University of Pennsylvania, which is supported by the NSF National Nanotechnology Coordinated Infrastructure Program under grant NSF–NNCI–2025608. The authors thank Prof. Karen I. Winey (Penn) for use of the potentiostat–frequency response analyzer in her lab, and Prof. Nigel Clarke (University of Sheffield) and Prof. Yue Qi (Brown University) for useful suggestions. The authors also thank Dr. Jamie Ford (Penn) for his useful suggestions regarding the ToF–SIMS data.

References

1. Alexandris, S., Papadopoulos, P., Sakellariou, G., Steinhart, M., Butt, H.J. and Floudas, G., **2016**. Interfacial Energy and Glass Temperature of Polymers Confined to Nanoporous Alumina. *Macromolecules*, *49*(19), pp.7400-7414. https://doi.org/10.1021/acs.macromol.6b01484.
2. Napolitano, S., Glynos, E. and Tito, N.B., **2017**. Glass Transition of Polymers in Bulk, Confined Geometries, and Near Interfaces. *Reports on Progress in Physics*, *80*(3), p.036602. https://doi.org/10.1088/1361-6633/aa5284.
3. Sharma, R.P. and Green, P.F., **2017**. Role of “Hard” and “Soft” Confinement on Polymer Dynamics at the Nanoscale. *ACS Macro Letters*, *6*(9), pp.908-914. https://doi.org/10.1021/acsmacrolett.7b00374.
4. Adrjanowicz, K., Winkler, R., Dzienia, A., Paluch, M. and Napolitano, S., **2019**. Connecting 1D and 2D Confined Polymer Dynamics to its Bulk Behavior via Density Scaling. *ACS Macro Letters*, *8*(3), pp.304-309. https://doi.org/10.1021/acsmacrolett.8b01006.
5. Maguire, S.M., Bilchak, C.R., Corsi, J.S., Welborn, S.S., Tsaggaris, T., Ford, J., Detsi, E., Fakhraai, Z. and Composto, R.J., **2021**. Effect of Nanoscale Confinement on Polymer-Infiltrated Scaffold Metal Composites. *ACS Applied Materials & Interfaces*, *13*(37), pp.44893-44903. https://doi.org/10.1021/acsami.1c12491.
6. Krutyeva, M., Wischnewski, A., Monkenbusch, M., Willner, L., Maiz, J., Mijangos, C., Arbe, A., Colmenero, J., Radulescu, A., Holderer, O., Ohl, M., and Richter, D., **2013**. Effect of Nanoconfinement on Polymer Dynamics: Surface Layers and Interphases. *Physical Review Letters*, *110*(10), p.108303. https://doi.org/10.1103/PhysRevLett.110.108303.

7. Chrissopoulou, K. and Anastasiadis, S.H., **2015**. Effects Of Nanoscopic-Confinement on Polymer Dynamics. *Soft Matter*, *11*(19), pp.3746-3766. https://doi.org/10.1039/C5SM00554J.
8. Richter, D. and Kruteva, M., **2019**. Polymer Dynamics Under Confinement. *Soft Matter*, *15*(37), pp.7316-7349. https://doi.org/10.1039/C9SM01141B.
9. Barroso-Bujans, F., Fernandez-Alonso, F., Pomposo, J.A., Cerveny, S., Alegría, A. and Colmenero, J., **2012**. Macromolecular Structure and Vibrational Dynamics of Confined Poly (ethylene oxide): From Subnanometer 2D-Intercalation into Graphite Oxide to Surface Adsorption onto Graphene Sheets. *ACS Macro Letters*, *1*(5), pp.550-554. https://doi.org/10.1021/mz3001012.
10. Zhang, T., Winey, K.I. and Riggleman, R.A., **2018**. Polymer Conformations and Dynamics Under Confinement with Two Length Scales. *Macromolecules*, *52*(1), pp.217-226. https://doi.org/10.1021/acs.macromol.8b01779.
11. Guan, Y., Liu, G., Gao, P., Li, L., Ding, G. and Wang, D., **2013**. Manipulating Crystal Orientation of Poly(ethylene oxide) by Nanopores. *ACS Macro Letters*, *2*(3), pp.181-184. https://doi.org/10.1021/mz300592v.
12. Zhang, Z., Ding, J., Ocko, B.M., Lhermitte, J., Strzalka, J., Choi, C.H., Fisher, F.T., Yager, K.G. and Black, C.T., **2020**. Nanoconfinement and Salt Synergistically Suppress Crystallization in Polyethylene Oxide. *Macromolecules*, *53*(4), pp.1494-1501. https://doi.org/10.1021/acs.macromol.9b01725.
13. Liu, G., Muller, A.J. and Wang, D., **2021**. Confined Crystallization of Polymers within Nanopores. *Accounts of Chemical Research*, *54*(15), pp.3028-3038. https://doi.org/10.1021/acs.accounts.1c00242.
14. Zhang, Z., Ding, J., Ocko, B.M., Fluerasu, A., Wiegart, L., Zhang, Y., Kobrak, M., Tian, Y., Zhang, H., Lhermitte, J. and Choi, C.H., **2019**. Nanoscale Viscosity of Confined Polyethylene Oxide. *Physical Review E*, *100*(6), p.062503. https://doi.org/10.1103/PhysRevE.100.062503.
15. Wang, H., Qiang, Y., Shamsabadi, A.A., Mazumder, P., Turner, K.T., Lee, D. and Fakhraai, Z., **2019**. Thermal Degradation of Polystyrene Under Extreme Nanoconfinement. *ACS Macro Letters*, *8*(11), pp.1413-1418. https://doi.org/10.1021/acsmacrolett.9b00649.
16. Ma, H., Lionti, K., Magbitang, T.P., Gaskins, J., Hopkins, P.E., Huxtable, S.T. and Tian, Z., **2021**. Pore-Confined Polymers Enhance the Thermal Conductivity of Polymer Nanocomposites. *ACS Macro Letters*, *11*(1), pp.116-120. https://doi.org/10.1021/acsmacrolett.1c00703.
17. Horowitz, Y., Strauss, E., Peled, E. and Golodnitsky, D., **2021**. How to Pack a Punch–Why 3D Batteries are Essential. *Israel Journal of Chemistry*, *61*(1-2), pp.38-50. https://doi.org/10.1002/ijch.202100001.
18. Lascaud, S., Perrier, M., Vallee, A., Besner, S., Prud'Homme, J. and Armand, M., **1994**. Phase Diagrams and Conductivity Behavior of Poly(ethylene oxide)-Molten Salt Rubbery Electrolytes. *Macromolecules*, *27*(25), pp.7469-7477. https://doi.org/10.1021/ma00103a034.

19. Bocharova, V. and Sokolov, A.P., **2020**. Perspectives for Polymer Electrolytes: A View from Fundamentals of Ionic Conductivity. *Macromolecules*, *53*(11), pp.4141-4157. https://doi.org/10.1021/acs.macromol.9b02742.
20. Song, Z., Chen, F., Martinez-Ibañez, M., Feng, W., Forsyth, M., Zhou, Z., Armand, M. and Zhang, H., **2023**. A Reflection on Polymer Electrolytes for Solid-State Lithium Metal Batteries. *Nature Communications*, *14*(1), p.4884. https://doi.org/10.1038/s41467-023-40609-y.
21. Cheng, S., Smith, D.M. and Li, C.Y., **2014**. How Does Nanoscale Crystalline Structure Affect Ion Transport in Solid Polymer Electrolytes? *Macromolecules*, *47*(12), pp.3978-3986. https://doi.org/10.1021/ma500734q.
22. Zheng, F., Li, C., Li, Z., Cao, X., Luo, H., Liang, J., Zhao, X. and Kong, J., **2023**. Advanced Composite Solid Electrolytes for Lithium Batteries: Filler Dimensional Design and Ion Path Optimization. *Small*, *19*(21), p.2206355. https://doi.org/10.1002/smll.202206355.
23. Huang, Y.R., Jiang, Y., Hor, J.L., Gupta, R., Zhang, L., Stebe, K.J., Feng, G., Turner, K.T. and Lee, D., **2015**. Polymer Nanocomposite Films with Extremely High Nanoparticle Loadings via Capillary Rise Infiltration (CaRI). *Nanoscale*, *7*(2), pp.798-805. https://doi.org/10.1039/C4NR05464D.
24. Venkatesh, R.B., Manohar, N., Qiang, Y., Wang, H., Tran, H.H., Kim, B.Q., Neuman, A., Ren, T., Fakhraai, Z., Riggleman, R.A. and Stebe, K.J., **2021**. Polymer-Infiltrated Nanoparticle Films Using Capillarity-Based Techniques: Toward multifunctional coatings and membranes. *Annual Review of Chemical and Biomolecular Engineering*, *12*, pp.411-437. https://doi.org/10.1146/annurev-chembioeng-101220-093836.
25. Lucas, R., **1918**. Ueber das Zeitgesetz des kapillaren Aufstiegs von Flüssigkeiten. *Kolloid-Zeitschrift*, *23*(1), pp.15-22. https://doi.org/10.1007/BF01461107.
26. Washburn, E.W., **1921**. The Dynamics of Capillary Flow. *Physical Review*, *17*(3), p.273. https://doi.org/10.1103/PhysRev.17.273.
27. Ratner, M.A. and Shriver, D.F., **1988**. Ion Transport in Solvent-Free Polymers. *Chemical Reviews*, *88*(1), pp.109-124. https://doi.org/10.1021/cr00083a006.
28. Mankovsky, D., Lepage, D., Lachal, M., Caradant, L., Aymé-Perrot, D. and Dollé, M., **2020**. Water Content in Solid Polymer Electrolytes: The Lost Knowledge. *Chemical Communications*, *56*(70), pp.10167-10170. https://doi.org/10.1039/D0CC03556D.
29. Devaux, D., Bouchet, R., Glé, D. and Denoyel, R.J.S.S.I., **2012**. Mechanism of Ion Transport in PEO/LiTFSI Complexes: Effect of Temperature, Molecular Weight and End Groups. *Solid State Ionics*, *227*, pp.119-127. https://doi.org/10.1016/j.ssi.2012.09.020.
30. Zhang, H., Liu, C., Zheng, L., Xu, F., Feng, W., Li, H., Huang, X., Armand, M., Nie, J. and Zhou, Z., **2014**. Lithium bis(fluorosulfonyl)imide/Poly(ethylene oxide) Polymer Electrolyte. *Electrochimica Acta*, *133*, pp.529-538. https://doi.org/10.1016/j.electacta.2014.04.099.
31. Mongcopa, K.I.S., Tyagi, M., Mailoa, J.P., Samsonidze, G., Kozinsky, B., Mullin, S.A., Gribble, D.A., Watanabe, H. and Balsara, N.P., **2018**. Relationship between Segmental

Dynamics Measured by Quasi-Elastic Neutron Scattering and Conductivity in Polymer Electrolytes. *ACS Macro Letters*, *7*(4), pp.504-508. https://doi.org/10.1021/acsmacrolett.8b00159.

32. Pesko, D.M., Sawhney, S., Newman, J. and Balsara, N.P., **2018**. Comparing Two Electrochemical Approaches for Measuring Transference Numbers in Concentrated Electrolytes. *Journal of The Electrochemical Society*, *165*(13), pp.A3014-A3021. https://doi.org/10.1149/2.0231813jes.
33. Zhao, Y., Tao, R. and Fujinami, T., **2006**. Enhancement of Ionic Conductivity of PEO-LiTFSI Electrolyte Upon Incorporation of Plasticizing Lithium Borate. *Electrochimica Acta*, *51*(28), pp.6451-6455. https://doi.org/10.1016/j.electacta.2006.04.030.
34. Xiong, Z., Wang, Z., Zhou, W., Liu, Q., Wu, J.F., Liu, T.H., Xu, C. and Liu, J., **2023**. 4.2 V Polymer All-Solid-State Lithium Batteries Enabled by High-Concentration PEO Solid Electrolytes. *Energy Storage Materials*, *57*, pp.171-179. https://doi.org/10.1016/j.ensm.2023.02.008.
35. Hoffman, Z.J., Shah, D.B. and Balsara, N.P., **2021**. Temperature and Concentration Dependence of the Ionic Transport Properties of Poly (ethylene oxide) Electrolytes. *Solid State Ionics*, *370*, p.115751. https://doi.org/10.1016/j.ssi.2021.115751.
36. Cai, J. and Yu, B., **2011**. A Discussion of The Effect of Tortuosity on the Capillary Imbibition in Porous Media. *Transport in Porous Media*, *89*(2), pp.251-263. https://doi.org/10.1007/s11242-011-9767-0.
37. Ghanbarian, B., Hunt, A.G., Ewing, R.P. and Sahimi, M., **2013**. Tortuosity in Porous Media: A Critical Review. *Soil Science Society of America Journal*, *77*(5), pp.1461-1477. https://doi.org/10.2136/sssaj2012.0435.
38. Ishitani, T., Umemura, K., Ohnishi, T., Yaguchi, T. and Kamino, T., **2004**. Improvements in performance of focused ion beam cross-sectioning: aspects of ion-sample interaction. *Microscopy*, *53*(5), pp.443-449. https://doi.org/10.1093/jmicro/dfh078.
39. Fearn, S., **2015**. *An Introduction to Time-Of-Flight Secondary Ion Mass Spectrometry (ToF-SIMS) And its Application to Materials Science*. Morgan & Claypool Publishers. https://doi.org/10.1088/978-1-6817-4088-1ch4.
40. Tu, C.H., Veith, L., Butt, H.J. and Floudas, G., **2022**. Ionic Conductivity of a Solid Polymer Electrolyte Confined in Nanopores. *Macromolecules*, *55*(4), pp.1332-1341. https://doi.org/10.1021/acs.macromol.1c02490.
41. Hernández, G., Lee, T.K., Erdélyi, M., Brandell, D. and Mindemark, J., **2023**. Do Non-Coordinating Polymers Function as Host Materials for Solid Polymer Electrolytes? The Case of PVdF-HFP. *Journal of Materials Chemistry A*, *11*(28), pp.15329-15335. https://doi.org/10.1039/D3TA01853A.
42. Tekell, M.C., Nikolakakou, G., Glynos, E. and Kumar, S.K., **2023**. Ionic Conductivity and Mechanical Reinforcement of Well-Dispersed Polymer Nanocomposite Electrolytes. *ACS Applied Materials & Interfaces*, *15*(25), pp.30756-30768. https://doi.org/10.1021/acsami.3c04633.

43. Martín Dalmas, J., van Roekeghem, A., Mingo, N. and Mossa, S., **2024**. Can Silica Nanoparticles Improve Lithium Transport in Polymer Electrolytes? *The Journal of Physical Chemistry C*. https://doi.org/10.1021/acs.jpcc.3c08080.

Table of Contents (ToC) Graphic